Babes-Bolyai University
Faculty of Physics

-Doctoral thesis summary-

The study of thin films and nanoparticles of doped ZnO materials

by
Maria-Iuliana Toma

Scientific Advisor
Prof. Dr. Aurel Pop

Cluj-Napoca, 2021

Table of contents

Keywords: doped zinc oxide nanostructures, aluminium and gallium, rare earths-RE (neodymium, gadolinium, erbium), structural properties, optical and electrical properties

Introduction

The high overall environmental pollution and the accentuated greenhouse gases has driven researchers and industries to replace conventional fossil fuels with alternative energy sources and modern filtering methods which are more environmentally friendly and economically favourable **[1-3]**. Our daily lives depend on various forms of energy whether we drive cars, operate machines, or even see after dark. However, this is also one of the leading issues in the "Top Ten" global concerns **[4]**. Thus, clean and renewable energy alternatives for a low-carbon future are most important nowadays. Because renewable energy resources have always been in demand, semiconductor materials are one promising solution to utilize for solar energy in photovoltaic devices **[5,6]**.

Recent research in materials science over zinc oxide have resulted in enormous progress in commercializing nano technologies that use renewable energy. Moreover, emerging strategies for the use of sophisticated nano-systems or devices are rapidly changing. This started with the electronics industry, where new goals and better solution were provided with the help of nanotechnology **[7]**. For developing nano-electronic and optoelectronic devices, nano-electronics has focused on the optical, structural, magnetic and photoluminescence properties of the nanostructures **[8]**. These properties have a very important role at the nano-scale level compared to the bulk compounds.

Another relatively new class of materials with practical applications in the field of sensors, electronic components, as well as in the field of bio-medicine, is represented by thin organic films, which have a key role in the coverage of chemical and biochemical sensors, electronic devices, development of new generation and acquiring layers of passivation. Due to the possibility of large-scale production of electronic devices at lower costs, these type of films contributes to the manufacture of batteries, transistors, organic dielectrics with high performance and optical devices for data storage **[9]**.

Motivation and thesis outline

The aim of this thesis was to investigate the morpho-structural, optical and electrical characteristics of ZnO thin films and nanoparticles, respectively. In order to obtain the 2D films, RF magnetron sputtering (at a temperature of 150°C) was used. For the nanostructures a soft chemical method was developed. After we established synthesis parameters, we first added Ga and Al elements to the ZnO films in order to evaluate the different influence upon structural, optical and electrical properties of the

films. Thus, the doping elements were added to the ZnO host material individually and together (Ga+Al). The second step was to add various RE dopants (Nd, Gd, Er) and Ga to the primary host material, ZnO. By this, we wanted to improve both optical and electrical properties by co-doping with Ga and RE.

The novelty of this work has started from the idea of doping ZnO thin films with various elements (Al+Ga) in order to increase conductivity and in order to improve transparency we added RE elements with the aim of having suitable materials for optoelectronic devices and photovoltaics. Nevertheless, another interesting idea was to use 4f elements doped ZnO nanostructures and then evaluate the changes in their photoluminescence, size and crystallinity. To keep the consistency of this work, we chose the same lanthanides for doping the ZnO nanoparticles as in the case of thin films. Thus, we focused on the unique and distinct semiconducting properties of rare-earth-doped ZnO nanostructures with regard to applied sciences. Furthermore, ZnO materials are more resistant to radiation damage than other common semiconductor materials, like Si, GaAs, CdS, and even GaN; therefore, it should be useful for space applications **[10]**. Following from and adding to this brief discussion of 0D and 2D materials, the thesis is divided into six chapters including the introduction.

Chapter 1 provides an overview of the current research trends. Also here, the main properties of the main material, ZnO are described, as well as the doping elements we chose to work with (Al, Ga, Nd, Gd, Er). **Chapter 2** covers the characterization of structural, optical and electrical properties for doped ZnO thin films, as well as the characterization techniques for the prepared RE-doped ZnO nanoparticles. **Chapter 3** presents detailed synthesis techniques for both nanoparticles and thin films. Furthermore, the operating conditions for the thin film systems and the main steps and precursors used to synthesize the nanostructures were explained. **Chapter 4** gives information about the Ga-doped ZnO thin films (GZO) and the (Al+Ga) co-doped ZnO thin films (AGZO) taking into consideration the analysis of the crystallographic results of the targets used for sputtering the films afterwards. Additional characterization techniques were used to determine the surface, optical and electrical properties. **Chapter 5** describes the influence of RE-doped GZO thin films (Nd-GZO, Gd-GZO, Er-GZO) upon structural, optical and electrical properties. **Chapter 6** encompass the structural and optical properties of the RE-doped ZnO nanostructures synthesized by a wet chemical method. In the end a summary of the results is given with concluding remarks.

Chapter 1. General properties of ZnO and state of the art

1.1. Literature overview. Nanoparticles and 2D materials

The most common representation of zero-dimensional (no dimension, or 0D) materials are nanoparticles. They are nanomaterials wherein all the dimensions are measured within the nanoscale, usually below 100 nm **[11]**. Nanoparticles can be amorphous, crystalline or polycrystalline and their composition can consist of multi-chemical elements. They can be metallic, ceramic or polymeric and they can take various shapes and forms. Quantum-sized nanostructures can exist individually or they can be incorporated in a matrix. In the case of metals and semiconductors the electronic wave functions of conduction electrons are delocalised over the entire particle **[12]**. Furthermore, when the dimensions of bulk crystalline materials are reduced to the nanoscale the overall behaviour changes. Quantum confinement involves restricting the motion of a particle within a particular volume. When the size of the particle is comparable to the volume, then the available energy states become discrete and for charge carriers in semiconductor materials, the effective band gap between valence and conduction bands increases. Thus, if the semiconductor is strongly confined in all three directions, then a QD is created (0D nanomaterial) and no electron delocalization occurs **[13]**. In the case of 2D materials, the conduction electron will be confined across the thickness but delocalized in the plane of the layer. To entail this quantum effect, for 0D materials the electrons are fully confined, while for 2D materials electron confinement and delocalization coexist (this quantum effect is also available for 1D materials) **[14]**.

On the other hand, thin films are 2D materials obtained by using different chemical or physical techniques attached to supports defined as substrates. The properties within films are different from those of the same materials in bulk form. Due to their decreased dimensions, geometry, grain size, lattice defects, voids and other characteristics which are more predominant in thin films compared to the bulk material. The thin surfaces of a film are so close to each other resulting in a strong influence on the film's internal physical properties. These unique properties give rise to various applications. Nowdays our knowledge has expanded towards the atomic scales making our lives benefit from all the innovations: smart cell phones with touch screens, various biomedical applications, stacked organic solar cells, and many others **[15]**.

1.2. ZnO properties and doping importance

ZnO belongs to binary II-VI group of semiconductors with large exciton binding energy (E ~ 60 meV), that can crystallize into the wurtzite, zincblende, or rocksalt structures, as illustrated in Figure 1.3.1. Besides that, ZnO is formed by tetrahedral (sp^3) bonding, while its wurtzite structure is the most stable form at room temperature and is from hexagonal crystal system. This wurtzite structure consists of two interpenetrating hexagonal-close-packed (hcp) sublattices, where each sublattice includes four atoms per unit cell and every atom of one kind (group II atom) is surrounded by four atoms of the other kind (group VI) or vice versa, which are coordinated at the edges of a tetrahedron (Figure 1.3.1). However, when reduced to the nanoscale, its properties become very size and structure dependent. This means that by changing the morphological conditions during the synthesis process we can produce a wide variety of structures that are finely tuned in properties, due to the quantum confinement effect **[16]**. Moreover, the process of doping and/or co-doping can improve various properties of the host material from optical to electrical characteristics that could make the final material suitable for applications. It is well known that the addition of defect states or impurities into the semiconductor lattices is the primary means of controlling optical, luminescent, electrical conductivity, magnetic, and other physical properties.
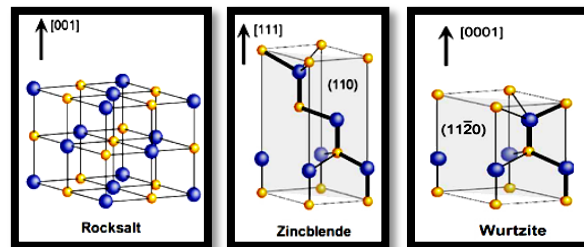
Fig.1.3.1 Representation of ZnO crystallographic structures, from left to right: rocksalt (cubic), Zinc-blende, hexagonal wurtzite. The yellow spheres denote the Zn and the blue spheres represent oxigen atoms **[17]**

Both Al and Ga are part of the same group of elements with close ionic radius values to that of Zn, which makes the substitution of Zn atoms from the lattice favourable. Also, by doping ZnO material with each of these two elements, Al and Ga elements result in n-type semiconductors. On the other hand, because of the free electrons from the 4f state, RE elements show unique properties when combined with materials with a 3d electrochemical structure state, creating photoluminescent centres.

In terms of their importance in doping, both Al_2O_3 and Ga_2O_3 were used to improve the electrical conductivity of the final films. However, in order to improve optical properties, RE, such as, Nd_2O_3, Gd_2O_3 and Er_2O_3 were chosen [18]. Rare earth ions are intensively investigated concerning their optical and unique spectroscopic properties due to their electronic configurations. Their partially filled 4f electrons are responsible for the characteristic optical transitions properties for RE^{3+}. These 4f orbitals have different energies exhibiting rich energy level structure, wavelength covering from UV-vis to IR part of the spectrum.

To be able to use ZnO nanoparticles in sophisticated applications, the optimum solution for enhancing the performance properties of ZnO without changing its physical-chemical properties is required. Nevertheless, to enhance the properties of ZnO nanostructures, we have to add impurities or defects at the time of their synthesis. In ZnO nanostructures, there are two types of defects: intrinsic defects and extrinsic defects.

1.3. General methods in obtaining thin layers and nanoparticles

Thin films can be obtained by various methods, for example: chemical deposition and physical deposition. One of the most widely used growth techniques for ZnO films is sputtering. The availability of many parameters that control sputter deposition makes it a complex process, with a large degree of control over the growth and microstructure of the film. In the beginning, only DC (direct current) sputtering was used to grow ZnO films from a Zn target in an Ar and O gas mixture. However, the DC diodes are inadequate for the deposition because of slow deposition rates, high voltages, and low currents. In order to avoid these disadvantages, a radio frequency (RF) power supply has been emerged to replace the DC power supply which eliminates the charging problems.

In terms of NP formation there can be various physical, chemical, biological or hybrid methods [19]. Nanoparticles can be prepared from any solid or liquid material, including metals, dielectrics, and semiconductors. The most common synthesis examples of solution-based approaches to synthesize ZnO nanostructures include hydrothermal, sol-gel, precipitation, electrochemical deposition process, wet chemical method and others.

Chapter 2. Characterization techniques for thin films and nanoparticles

2.1. X-ray diffraction (XRD)

X-ray diffraction (XRD) is a technique used to characterize the crystal structure, grain size, and preferred orientation in crystalline samples. A beam of X-rays strike a sample interacting with crystal planes resulting in a diffraction pattern for constructive interactions that follow Bragg's Law:

$$n \cdot \lambda = 2d \cdot \sin\theta$$

where n is the order of diffraction, λ is the X-ray wavelength, d is the interplanar spacing of crystal planes, and θ is the incident angle of X-ray.

The film structure was characterized by XRD analysis, using a Brucker D8 X-ray diffractometer with a CuK$_\alpha$ radiation ($\lambda_{CuK\alpha} = 0.15406$ nm). The crystal phases were identified by comparing the 2θ values and intensities of reflections on X-ray diffractograms with JCP data base using the Diffraction AT-Brucker program. The thin film measurements were taken under the same parameter scans performed between 2θ values of 20° – 80°, with a typical acquisition step of 0.02 / 5 seconds time and 12 rpm. The parameters used to measure the targets were the following: 2θ values of 20° – 80°, acquisition step 0.1 / 5 seconds time and 12 rpm.

The XRD peaks were fitted using a Lorentzian function (equation 2.1.1) of the Origin2017 program

$$F(x) = \frac{2 \cdot A}{\pi} \cdot \frac{w}{4 \cdot (x - x_0)^2 + w^2} \quad (2.1.1)$$

Here A, x_0 and w are the peak area, position of the peak and full width at half maximum (FWHM). Additional information or changes can be found in each chapter.

The influence of substrate–target distance, d, on the stress along the c-axis direction for all thin films was investigated by using the biaxial strain model, for the hexagonal lattice of ZnO, the stress (σ) in the film was calculated by the following formula:

$$\sigma = \frac{2c_{13}^2 - c_{33}(c_{11} + c_{12})}{2c_{13}} \times \varepsilon \quad (2.1.2)$$

where ε is the unstrained lattice parameter (American Society for Testing and Materials), having the formula:

$$\varepsilon(\%) = \frac{(c_{film} - c_{bulk})}{c_{bulk}} \times 100 \quad (2.1.3)$$

where c_{bulk} = 0.5206 nm and c_{film} is measured by XRD. By using the elastic constants c_{ij} of single-crystalline ZnO from reference [20], we obtain σ_{film} = −233 × ε (GPa). This compressive stress takes place during deposition process itself.

2.2. Atomic force microscopy (AFM)

AFM is a tool used to characterize the surface topography and morphology of thin films. For all samples, intermittent contact mode (tapping mode) AFM was used to map out the topography of the film surface. In tapping mode, the cantilever oscillates near its resonance frequency. The tips used were purchased from Tipsnano, NSG 10 series, with a nominal tip radius between 8 – 10 nm. The average surface roughness (RMS) of all the films was estimated using WSXM5 software.

2.3. Raman spectroscopy

Raman spectroscopy is a versatile technique for fast and non-destructive study of dopant incorporation. The Raman spectra of all samples (thin films) were recorded using a Renishaw in Via Raman Microscope. The He-Ne laser with a power of 50 mW was used. The spectral resolution of the recorded spectra was approximately 4 cm^{-1}. For Raman measurements of (Ga+Al) doped ZnO the thin film samples a 40x objective, a wavelength of 532 nm – 2.33 eV (green excitation) and the 10% neutral density filter was used. The registered spectra are the average of 4 accumulations with 10 s integration time. For the rest of the thin film samples the He-Cd laser with a power of 50 mW was used. The registered spectra are the average of 4 accumulations with 10 s integration time, a 50x objective and UV excitation (325 nm – 3.81 eV) with the 2400 grating. Nevertheless, for the measurements of the NP in colloidal solution the spectra were taken using HORIBA LabRAM HR 800 spectrometer with a He-Cd laser excitation of 325 nm and with 2400 lines grating. The samples were measured in the liquid phase using Si(111) as a substrate. In order to minimize the heating effect, the laser power was kept below 50 µW under 40 x CaF2 objectives.

2.4. Transmission electron microscopy (TEM) and selected area electron diffraction (SAED)

TEM and SAED measurements were carried out on a Philips CM 20 FEG microscope at an accelerating voltage of 200 kV. TEM gives images of internal structure of a sample sufficiently thin (~100 nm) to allow transmission of electrons, typically

100 kV – 300 kV. Electron diffraction patterns give detailed crystallographic information, such as, crystal orientation, lattice parameters and sample thickness. SAED is referred to as "selected" because the user can easily choose from which part of the sample to obtain the diffraction pattern.

2.5. Transmittance spectroscopy and reflectance

Optical transmission measurements were done with a Carry 500 Spectrometer (300 nm – 1000 nm range). From the transmission spectra, the optical constants were calculated using the program PARAV-V2.0 **[21]**. Optical properties were emphasized by transmittance spectroscopy that showed values between 80% – 95% for the wavelength range between 350 nm to 1000 nm.

2.6. Photoluminescence (PL) and absorption measurements

Photoluminescence (PL) was registered on a Varian Cary Eclipse Fluorescence Spectrophotometer. To acquire PL spectra the samples were excited by 290 nm (4.27 eV) light in standard 10.0 mm quartz containers. The absorption profiles were registered using a Specord 220 Double beam spectrophotometer in 1.0 mm standard quartz containers using zinc(II) acetate solution in DMSO as a blank reference sample**.**

2.7. Resistivity measurements

The electrical conductivity of thin film is usually measured by four probe method. This technique involves bringing 4 equally spaced probes in contact with the material of unknown resistance. If the thickness of the sample is known, the equation used to determine the resistivity will be as follows:

$$\rho = \frac{\pi}{\ln 2} \cdot R \cdot t \quad (2.7.1)$$

where ρ is the resistivity, R is the resistance of the film measured at room temperature and t represents the thickness of the thin film.

For measuring the thin film samples we used the following parameters: I = 50 µA, ΔT = 1 K and the temperature decreased from room temperature (300 K) to 20 K.

Chapter 3. Synthesis tailoring and deposition parameters for thin films and nanoparticles

3.1. Thin film synthesis by RF magnetron sputtering technique

The reason for choosing RF sputtering method is due to its main advantages such as good reproducibility and uniform thickness of the obtained films, pinhole free thin films, and deposition over a large surface area owing to the high kinetic energy of the sputtered atoms on the substrate.

Sputtering sources often employ magnetrons that utilize strong electric and magnetic fields to confine charged plasma particles close to the surface of the sputtered target. Near the magnetron a magnetic field is produced and electrons follow helical paths around the field lines, resulting in the appearance of ring-shaped erosion on the surface of the target (Figure 3.1.1).

Fig.3.1.1 Ring-shaped erosion on the surface of the target

3.2. Target composition, thin film preparation and deposition parameters for the RF magnetron sputtering deposition

The target represents a round ceramic structure that contains: 5 g of compound from which: for doped ZnO thin films with Ga_2O_3: 98% weight percentage of ZnO and 2 wt% of Ga_2O_3. While, for co-doped ZnO thin films with Al_2O_3, Ga_2O_3: 97 wt% of ZnO, 2 wt% of Al_2O_3 and 1 wt% of Ga_2O_3. Moreover, for co-doped ZnO films with Ga_2O_3 and RE_2O_3: 97 wt% of ZnO, 2 wt% of Ga_2O_3 and 1 wt% of Gd_2O_3, Er_2O_3, and Nd_2O_3. All chemicals used where purchased from Sigma Aldrich (all with a purity grade of 99.9%).

For thin film deposition the following parameters were used: substrate temperature of 150°C and the deposition pressure was maintained at 2.1×10^{-2} mbar. The flux ratio for sputtering gas $F_{O2} = f_{O2} / (f_{Ar} + f_{O2})$ used was 0.375, the RF power density was 19.72 W / cm^2 and the deposition time was around 90 minutes. Meanwhile, 3 different distances between substrate-target were used during deposition, resulting in

a total of 16 samples (one pristine ZnO sample and 15 doped ZnO samples) shown in table 3.2.1.

Table 3.2.1 Samples details, parameters and types of analysis

Sample	Substrate-target distance, d (cm)	Composition, weight percentage (%)	Film thickness, t (nm)	Types of measurements
ZnO	6	100%	1000±0.1	XRD, Raman, Transmittance
GZO	4	98% ZnO + 2% Ga_2O_3	1552±0.1	XRD, AFM, Raman, Transmittance, Resistivity
	6		1015±0.1	
	8		687±0.1	
AGZO	4	97% ZnO + 2% Al_2O_3 + 1% Ga_2O_3	1686±0.2	XRD, AFM, Raman, Transmittance, Resistivity
	6		990±0.2	
	8		540±0.2	
Nd-GZO	4	97% ZnO + 2% Ga_2O_3 + 1% Nd_2O_3	2190±0.1	XRD, AFM, Raman, Transmittance, Resistivity
	6		900±0.2	
	8		565±0.1	
Gd-GZO	4	97% ZnO + 2% Ga_2O_3 + 1% Gd_2O_3	2133±0.1	XRD, AFM, Raman, Transmittance, Resistivity
	6		1036±0.1	
	8		552±0.1	
Er-GZO	4	97% ZnO + 2% Ga_2O_3 + 1% Er_2O_3	2019±0.2	XRD, AFM, Raman, Transmittance, Resistivity
	6		663±0.2	
	8		440±0.1	

3.3. Wet chemical method synthesis of nanoparticles

The chemicals used to prepare the nanoparticles were purchased from Sigma Aldrich: Zinc acetate (anhydrous), Erbium(III) nitrate hexahydrate, Neodymium(III) nitrate hexahydrate, and Gadolinium(III) nitrate hexahydrate (all with a purity grade of 99.9%). While, the solvents: tetraethylammonium hydroxide – TEA-OH (20% aqueous solution), dimethyl sulfoxide – DMSO (99+% purity), ethanol and tetrahydrofuran (THF) were purchased from Alfa Aesar. The synthesis was performed at ambient pressure by using Zn acetate and RE nitrates in DMSO solutions and aqueous TEA-OH.First, Zn acetate and each of RE nitrates were dissolved in DMSO to prepare solutions with concentrations of 1.0 mol% and 0.1 mol%. In the next step, 0.2 ml of the Zn acetate stock solution prepared above and 0.02 ml of the RE-dopant solution was diluted in 9.63 ml of DMSO. To this mixture, 0.15 ml of aqueous 20%TEA-OH was rapidly added while magnetic stirring. After this step, the final transparent colloidal solutions were subjected to heat treatment at 80°C for 60 minutes. TEM and SAED measurements of the samples, a purification step was required.

Chapter 4. The study of ZnO thin films doped with Ga and (Al+Ga)

4.1. Crystallographic analysis of the ZnO, GZO and AGZO targets and thin films

First, the XRD of the targets emphasize good crystallinity with clear peaks for each element phase (Figure 4.1.1). No intermediate crystal phases were formed which indicates that there are no new chemical phases related to Ga_2O_3 and $Al_2O_3+Ga_2O_3$ doping.
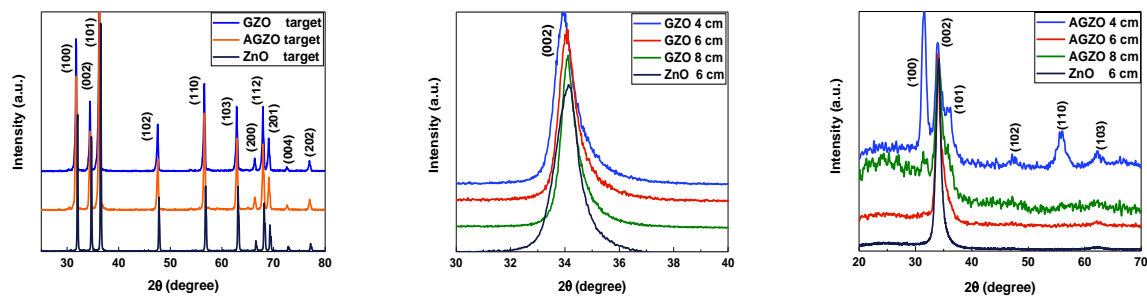

Fig.4.1.1 X-ray diffractograms recorded for ZnO, GZO and AGZO targets and films

Results for GZO films confirm a hexagonal wurtzite structure oriented perpendicular to the substrate surface, in the [001] crystallographic direction. This preferred orientation is due to the minimal surface energy of the (002) plane that corresponds to the dense packed plane of the ZnO hexagonal structure. By increasing the distance between substrate-target, d, from 4 cm to 8 cm, the intensity of (002) diffraction peak decreases as a result of the decrease of film thickness, and the unit cell height emphasis a small increase from c = 0.5237 nm to c = 0.5241 nm (Table 4.1.1).

Table 4.1.1 Structural parameters of ZnO, GZO and AGZO thin films

Sample	Substrate-target distance, d (cm)	Film thickness, t (nm)	Lattice parameter, c_{film} (nm)	Stress in the film, σ_{film} (GPa)	Crystallite size, D (nm)	Average roughness, RMS (nm)
ZnO	6	1000±0.1	0.5209	-0.40	26.4	
GZO	4	1552±0.1	0.5237	-1.65	15	35±0.1
	6	1015±0.1	0.5240	-1.79	14.5	23±0.1
	8	687±0.1	0.5241	-1.84	12	13±0.1
AGZO	4	1686±0.2	0.5248	-2.14	12.7	25±0.2
	6	990±0.2	0.5251	-2.28	12.6	22±0.2
	8	540±0.2	0.5251	-2.28	6	21±0.1

For d = 4 cm, the deposited AGZO films were polycrystalline, with (110), (002), (101), (102), (110) and (103) diffraction peaks of hexagonal ZnO. For d = 6 cm only the

(002) diffraction peak is present, suggesting that the structure is preferentially oriented along the c-axis. For d = 8 cm were present (101) and (110) diffraction peaks, but with much lower intensity compared to the c-axis (002) diffraction peak. The calculated stress **[22]** in the direction of the c-axis rises with increasing the distance between substrate-target for GZO highlighted in Table 4.1.1. This stress developed in the thin films is generally related to growth parameters, defects, impurities, and lattice distortion in the films. The lattice mismatch type of strain between film and substrate in these films is difficult to calculate due to the amorphous nature of glass substrate.The negative sign of the stress is the indication of compressive stress. Doping with Ga and co-doping with Al+Ga leads to the increase of compressive stress compared to the pristine ZnO film.

4.2. Topographic analysis of GZO and AGZO thin films

In the images below (Figures 4.2.1 and 4.2.2) the films show a compact and uniform surface, with spherical shaped grains, and revealed that the type of doping and the distance between substrate to target modified the microstructure of thin films.
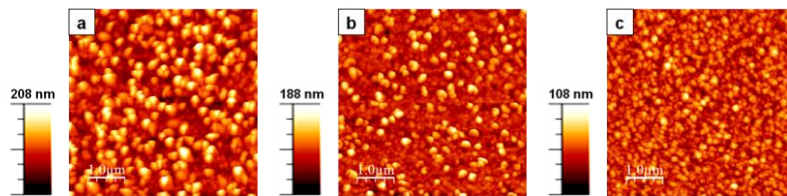

Fig.4.2.1 AFM measured micrographs for the GZO films deposited with varying substrate-target distance 4 cm, 6 cm, and 8 cm shown in a, b, and c respectively

For GZO films, the surface is composed of compact grain structures (Figure 4.2.1). By decreasing the distance between substrate-target here is an increase in the mean average roughness (Table 4.1.1). AGZO films exhibits a uniform surface as well as a high compact structure showing the typical density. Additionally, there is a small decrease in the RMS values with increasing substrate-target distance, from 35 to 13 nm for GZO samples, and for AGZO samples, from 25 to 21 nm.
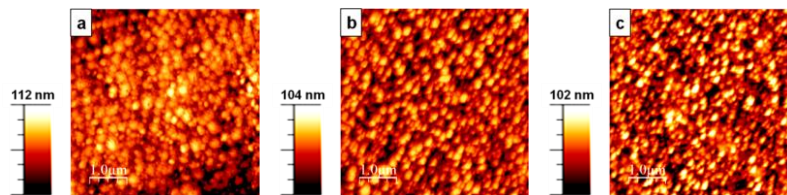

Fig.4.2.2 AFM measured micrographs for the AGZO films deposited with varying substrate-target distance 4 cm, 6 cm, and 8 cm shown in a, b, and c respectively

4.3. The study of GZO and AGZO thin films by Raman spectroscopy

Figure 4.3.1 show the Raman spectra of the pristine ZnO film, GZO, and AGZO thin films collected with the green excitation wavelength (532 nm). ZnO film (d = 6 cm) shows the peaks at 100 cm^{-1}, 273 cm^{-1}, 332 cm^{-1}, 436 cm^{-1} and 581 cm^{-1}. The peaks around 100 cm^{-1} and 436 cm^{-1} are attributed to both doubly degenerated $E_{2(low)}$ acoustic mode and high energy (optic) mode $E_{2(high)}$ phonons of the ZnO wurtzite structure. The peak at 273 cm^{-1} may be assigned to singly degenerated $B_{1(low)}$ acoustic vibrational mode, and the peak at 332 cm^{-1} to singly degenerated transverse-optic A_1(TO) mode. The peak at 581 cm^{-1} belongs to the longitudinal-optic LO's mode (overlapping of the E_1(LO) and A_1(LO) modes).
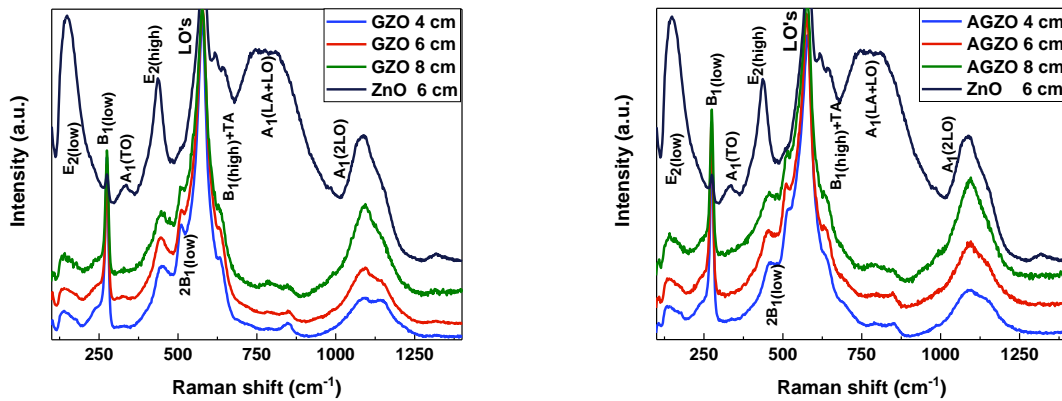

Fig.4.3.1 Raman spectra of ZnO, GZO, and AGZO thin films

Doping with Ga and Al+Ga introduces the single degenerated $2B_{1(low)}$ acoustic vibrational band and leads to the increase of intensity for LO's band, suggesting the increase of oxygen vacancies. The distance between substrate-target has influence only upon the shape of the last two broad second order bands. Due to the optical combinations, the broad band shows two local maxima at 1090 cm^{-1} and 1140 cm^{-1} for sample GZO (d = 4 cm) and a single asymmetric maximum at 1090 cm^{-1} for GZO (d = 8 cm).

4.4. Optical properties of GZO and AGZO thin films

For GZO samples (Figure 4.4.1), with decreasing d, the thickness of films increases, and the transmittance of the films decreases (from 90% for samples obtained at d = 6 cm and d = 8 cm to 83% for sample obtained at d = 4 cm). For AGZO (Figure 4.4.1) samples the distance between substrate-target of d = 6 cm and d = 8 cm does not affect significantly the optical absorption in the visible region (optical transmittance of about 91%).
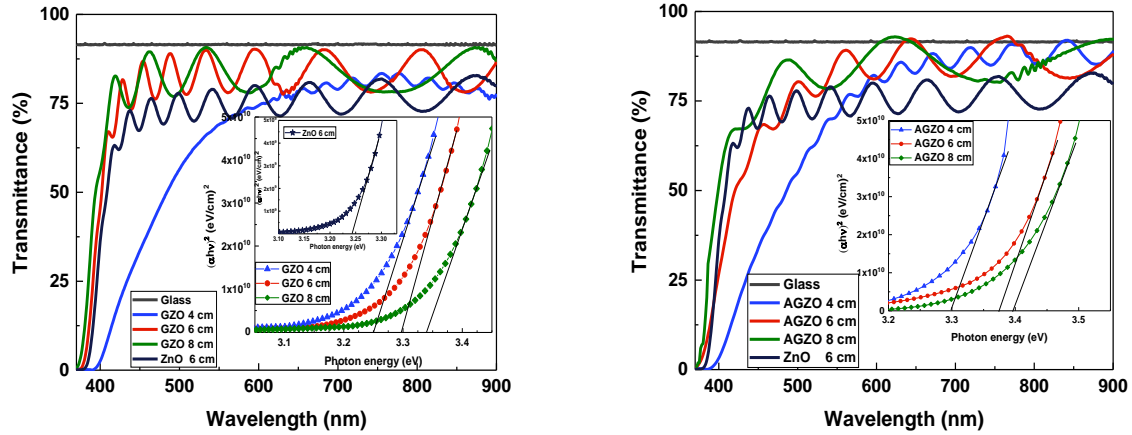
Fig.4.4.1 Transmittance spectra of reference substrate, ZnO, GZO, and AGZO thin films. The insert in each spectra represents the Tauc plot for three different distances

The band gap, E_g, was determined according to the Tauc relation (equation 4.4.1):

$$\alpha h\nu \;=\; A\big(h\nu - E_g\big)^{m} \quad (4.4.1)$$

where **A** is a constant called the band tailing parameter that depends on the electron-hole mobility, **h** is Planck's constant and **m** is the power transition mode, which is dependent upon the nature of the material, in our case is **½** (for direct allowed transitions). The optical absorption coefficient is defined as:

$$\alpha = \frac{1}{t}\ln\frac{(1-R)^{2}}{T} \quad (4.4.2)$$

where **t** is the thickness of the thin films and **R** and **T** are the reflectance and the transmittance, respectively. The optical band gap (E_g) was estimated by extrapolating the linear portion to the energy axis in the $(\alpha h\nu)^2$ vs. **hv** graph as emphasized in the inserted graphs in Figure 4.1.1. The optical band gap (E_g) was estimated by extrapolating the linear portion to the energy axis in the $(\alpha h v)^2$ vs. hv graph as emphasized in the Tauc plot inserts. By increasing d from 4 cm to 8 cm, the optical band gap (E_g) value increased from 3.26 eV to 3.34 eV for GZO and from 3.30 eV to 3.39 eV for AGZO, respectively. The increase in optical energy gap is due to the Burstein-Moss effect indicating the increase in structural disorders and defects. The incorporation of Al and Ga in the ZnO crystal structure decreased the crystallite size and increased residual stress of the thin films.

4.5. Electrical characterization of GZO and AGZO thin films

Samples below reveal the temperature-dependent resistivity curve, $\rho(T)$ and in the inserts represent $\ln(\rho)$ versus $1/T$ curves that fit reasonable the experimental data points in the specific temperature range for each sample.

GZO and AGZO samples exhibit similar transition trends that can be divided into two regions and an absolute minimum where the metal-semiconductor transition (MST) occurs. Thus, both samples show a metallic behaviour (from room temperature until the MST point) to semiconducting behaviour (from MST to 20 K). Both samples show a n-type characteristic with a resistivity below 10^{-3} $\Omega \times$ cm, which is attributed to good crystal quality of films and the displacement of Ga and Al atoms into Zn sites, providing extra free electrons into the conduction band.
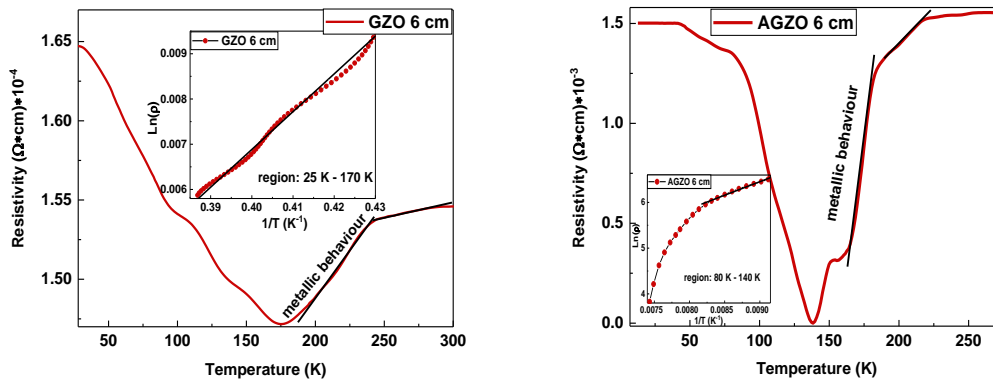

Fig.4.5.1 Temperature dependence of electrical resistivity of GZO and AGZO thin films. The insert shows the curve fit of experimental for the semiconducting behaviour

The observed metal–semiconductor transition (MST) in our ZnO doped films can be explained by a combined mechanism of carrier scattering (the metallic behaviour) and activation (semiconducting behaviour). The resistivity, **ρ** is given by:

$$\rho = \frac{1}{ne\mu} \quad (4.5.1)$$

where **n** is the carrier concentration, **e** is the electronic charge and **μ** is the mobility. The temperature dependence of electrical resistivity is related by the temperature dependences of mobility, **μ** and carrier concentration **n**, respectively. The competition between the mechanisms of activation and scattering of the carrier changes the function

of temperature. The main mechanism influencing the electron mobility in n-type doped ZnO thin films is electron scattering. The reciprocal mobility of the films can be expressed as

$$\frac{1}{\mu} = \frac{1}{\mu_g} + \frac{1}{\mu_l} + \frac{1}{\mu_i} \quad (4.5.2)$$

where μ_g, μ_l, and μ_i are the contribution to the mobility due to grain boundary scattering, lattice vibration scattering and ionized impurity scattering respectively.

By processing together the temperature dependence of mobility and the temperature dependence for mobility, the following equations are obtained:

$$n(T) = n_0 \left[1 + n_1 exp\left(\frac{E_g}{kT}\right) \right] \rightarrow \frac{1}{\mu} = B + CT^2 \quad (4.5.3)$$

where **B** and **C** are constants, while n_1 is a constant which is a measure of the relative contribution of carrier activation from native defects and E_g is the activation energy.

The metal–semiconductor transition was observed to have a changing point between 170 K and 175 K for the GZO film while for the AGZO film this transition is between 140 K and 165 K. This shift in resistivity could be assigned to the decreasing trend of the grain size for that leads to considerable grain boundary effects, which distributes their electrical properties. The resistivity, **ρ**, is inversely proportional to the product of carrier concentration, **n**, and the mobility, **μ**. Therefore the change in resistivity with different types of added dopants is due to change of **n** and/or **μ** which reflects in the film structure. The structural, morphological, vibrational and optical properties of the films have been found to be influenced by the distance between substrate to target.

Chapter 5. The study of ZnO thin films doped with Ga and RE elements

5.1. Crystallographic analysis of the RE-doped GZO targets and films

Compared to the pristine ZnO target, for the rest of the samples broader peaks are visible. The shift towards lower degree values emphasize that the dopants were successfully incorporated in the structure of the ZnO host material. The RE-doped GZO targets show two additional peaks around 28 degrees which are also shifted from one another. Additionally, for Nd doped GZO target a double peak around 30° occurs.
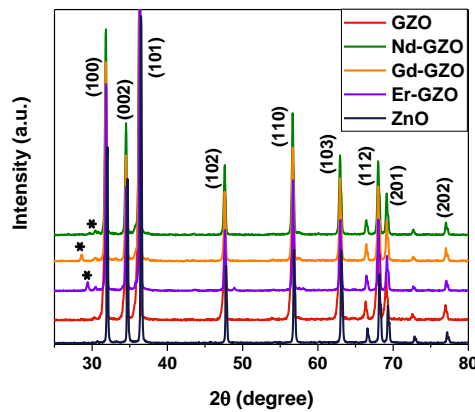

Fig.5.1.1 XRD pattern of ZnO, GZO and RE-doped GZO targets

Moreover, the incorporation of small amounts of RE-dopants into the host lattice results in additional peaks marked with asterisks (*) in Figure 5.1.1. RE-doping can cause distorted crystallinity of ZnO which may be to due to the large mismatch in ionic radius and charge imbalance between RE^{3+} and Zn^{2+}. However, in our case, most of the RE atoms are substituting Zn site as evident from the shift of the main diffraction peaks (100), (002), (101), (102), (110), (103), (112), (202) and very few of them are occupying interstitial sites. The shift towards higher angle side generally occurs when a dopant with higher ionic radii is substituted in place of host (ZnO) with lower ionic radii.

In the following figures XRD patterns for the RE-doped GZO thin films are discussed
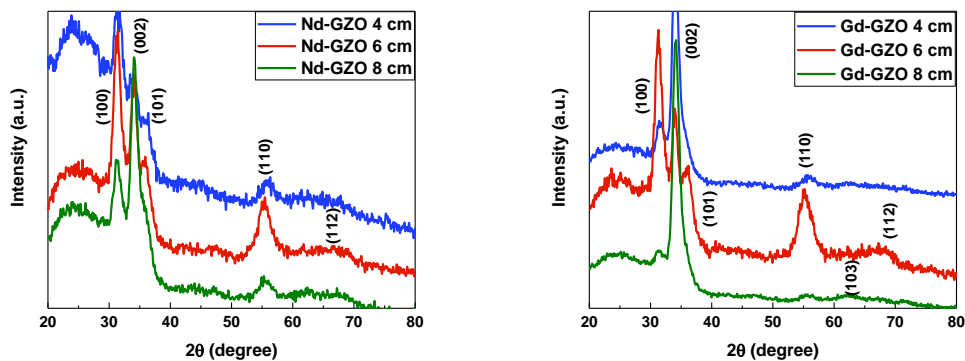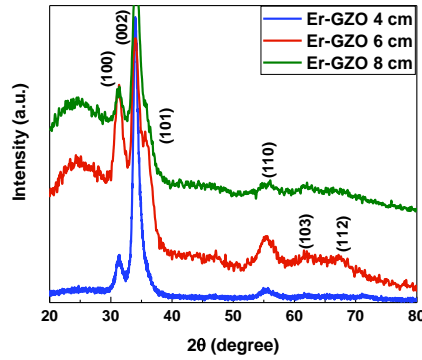
Fig.5.1.2 XRD pattern of Nd-GZO, Gd-GZO, and Er-GZO thin film for three deposition distances between substrate-target

Table 5.1.1 Film thickness, crystallite size and stress parameters of RE-GZO films

Sample	Substrate-target distance, d (cm)	Film thickness, t (nm)	Lattice parameter, c_{film} (nm)	Crystallite size, D (nm)	Stress in the film, σ_{film} (GPa)	Average roughness, RMS (nm)
Nd-GZO	4	2090±0.1	0.5512	10.41	-13.98	15±0.1
	6	740±0.2	0.5498	8.64	-13.35	10±0.1
	8	461±0.1	0.5491	6.85	-13.03	8±0.1
Gd-GZO	4	2028±0.1	0.5501	9.52	-13.48	14±0.1
	6	890±0.1	0.5509	10.3	-13.83	12±0.1
	8	453±0.1	0.5488	8.8	-12.90	11±0.1
Er-GZO	4	2013±0.2	0.5489	10.9	-12.94	25±0.1
	6	600±0.2	0.5506	7.21	-13.71	17±0.1
	8	471±0.1	0.5511	8.64	-13.93	7±0.1

It can be observed that for the RE-doped GZO thin films deposited at **6 cm** substrate-target distance, most of the diffraction peaks are clearly visible **(100)**, **(002)**, **(101)**, **(110)**, **(112),** compared to the films deposited at **4 cm** and **8 cm**, respectively. Taking into account all the RE-doped GZO films, the crystallinity evaluated from the intensity and full width at half-maximum of the **(002)** diffraction peak improved for the films deposited at **6 cm** substrate-target distance. This suggests that the **6 cm** substrate-target distance has more potential in manifesting better crystallinity throughout the film structure. Comparing the stress values in the case of the Ga-doped ZnO films with the RE-doped GZO films there is a noticeable increase in the last ones, reaching values of up to **-13.98 GPa**. This means that at least a fraction of the RE^{3+} ions is present in the ZnO crystallites and that these ions induce important stress in the ZnO matrix.

5.2. Topographic analysis of RE-doped GZO thin films

All samples emphasize a uniform and compact surface with spherical grains. The average roughness of the films is influenced by the type of dopants (Ga^{3+}, RE^{3+}) added to the ZnO host material. Moreover, all samples show a similar surface morphology, consisting of compact and well-defined grains.
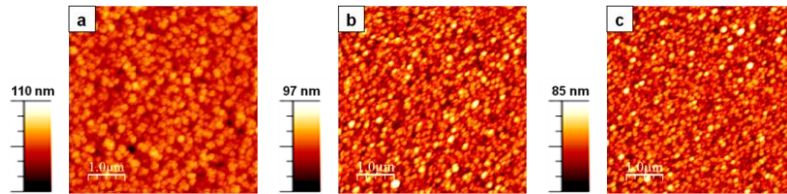

Fig.5.2.1 AFM measured micrographs for the Nd-GZO films deposited with varying substrate-target distance **4 cm**, **6 cm**, and **8 cm** shown in **a**, **b**, and **c** respectively

Fig.5.2.2 AFM measured micrographs for the Gd-GZO films deposited with varying substrate-target distance **4 cm**, **6 cm**, and **8 cm** shown in **a**, **b**, and **c**, respectively
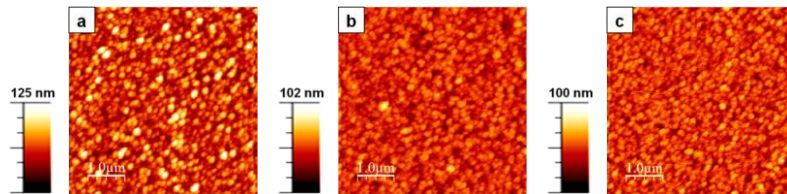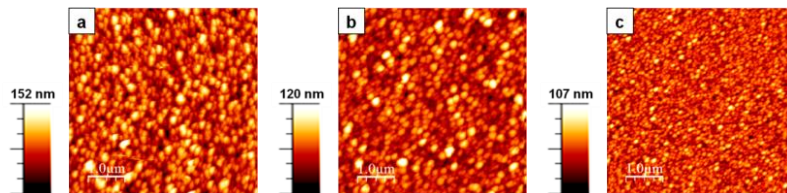

Fig.5.2.3 AFM measured micrographs for the Er-GZO films deposited with varying substrate-target distance **4 cm**, **6 cm**, and **8 cm** shown in **a**, **b**, and **c**, respectively

The root mean square (RMS) roughness for the thin films, calculated by using the AFM equipment's software is shown in Table 5.1.1. Furthermore, by adding RE^{3+} ions, they induce small distortions of the film surface structure. Also, depending on the type of RE^{3+} ion, differences upon the mean roughness is evidenced, with a small increase for the Er-doped GZO films compared to the Nd-GZO and Gd-GZO films, while keeping the same deposition conditions. The corresponding AFM images presented in figures above may be correlated to the previously studied structural characteristics.

5.3. The study of RE-doped GZO thin films by Raman spectroscopy

All samples show four intense major bands centred around, which mainly result from the polar symmetry modes $A_1(LO)$ and their overtones presented in figures blow.
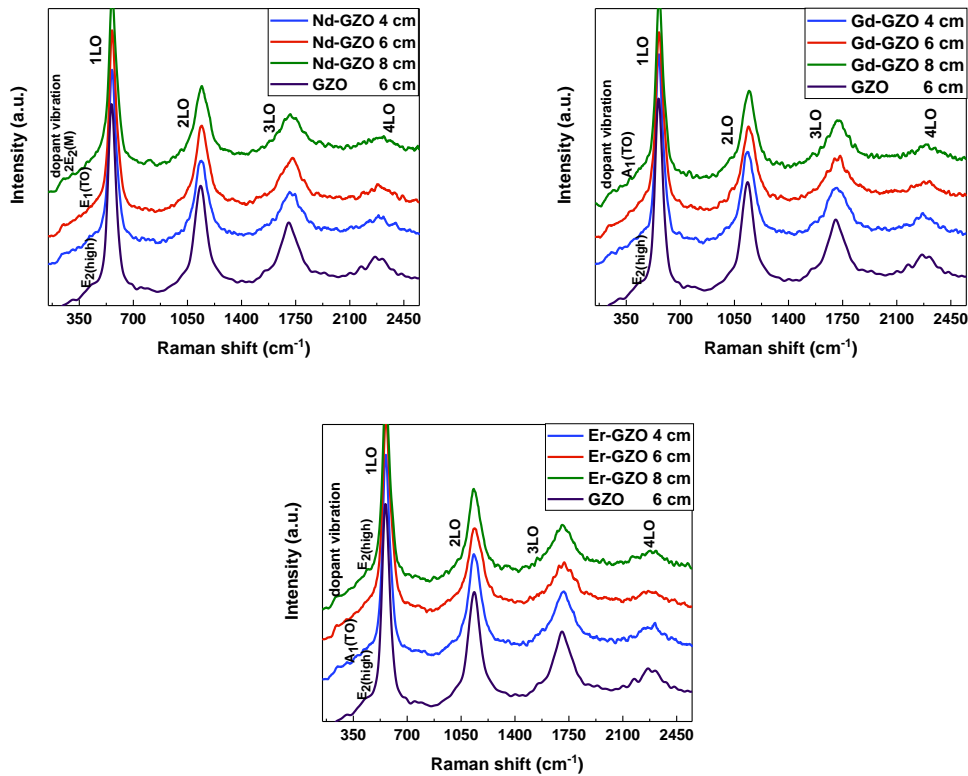

Fig.5.3.1 Raman spectra of Nd-GZO, Gd-GZO, and Er-GZO thin films deposited at three deposition distances between substrate-target

Taking into account all RE-doped samples, it is observed that the new dopant vibration modes' shapes are relatively broader and this aspect is related to the residual compressive strain. As explained earlier, the fact that the larger micro-strain in the lattice of RE-doped GZO films than Ga-doped ZnO films found from the XRD analysis is consistent with these additional broad Raman peaks. Therefore, it confirms that RE^{3+} ions occupy the Zn^{2+} positions because of the emerging new lattice defects.

5.4. Optical properties of RE-doped GZO thin films

Transmittance measurements emphasize that the RE-dopants have a strong influence on the optical properties. A slight increase in transmittance is observed in the case of Er-GZO films as compared to Nd-GZO and Gd-GZO films, possibly due to more

scattering of light of the Er element. All spectra show a high transparency in the visible range with a transmission above 85%.
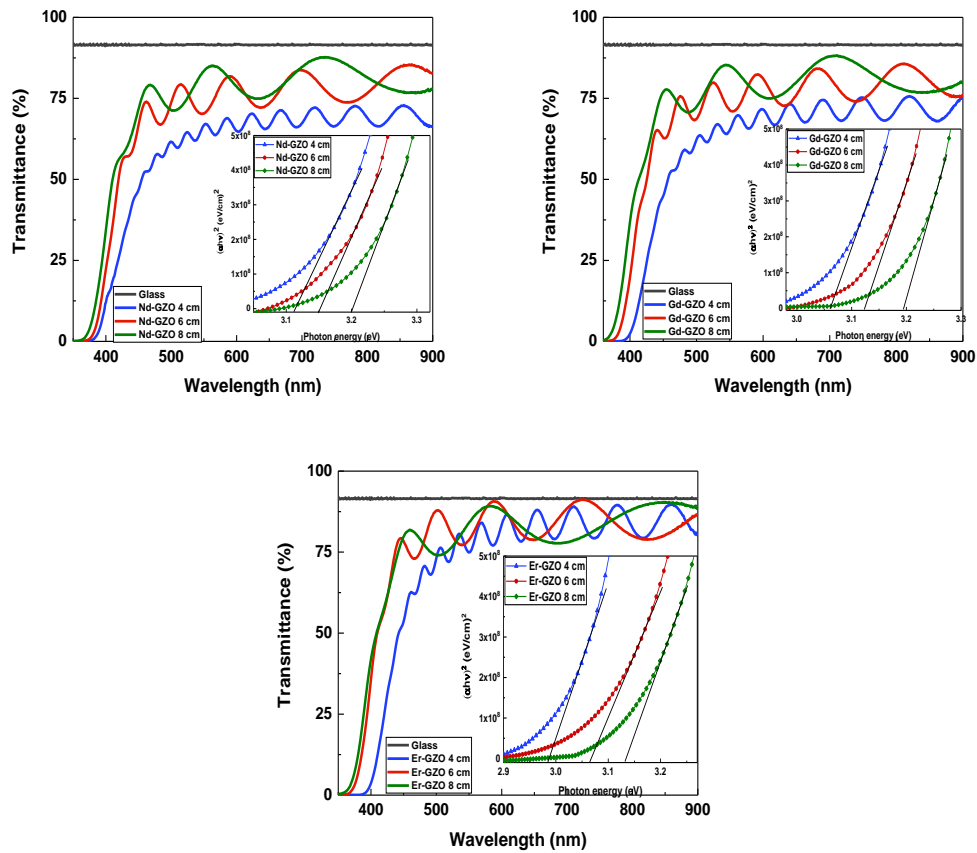

Fig.5.4.1 Transmittance results for Nd-GZO, Gd-GZO, and Er-GZO films and glass reference. The insert in each spectra represents the Tauc plot for three different distances

The optical band gap (E_g) was estimated by extrapolating the linear portion to the energy axis in the $(\alpha h\nu)^2$ vs. $h\nu$ graph **[23]** as emphasized in the Tauc plot inserts. The optical band gap values vary depending on the type of RE-dopant, between 2.98 eV and 3.20 eV, the lowest value belonging to Er-GZO sample deposited at 4 cm substrate-target distance. Also, the thickness values vary between 460 nm and 2090 nm, where the lowest values correspond to the Er-doped GZO samples.

5.5. Electrical characterization of RE-doped GZO thin films

Electrical resistivity, ρ, plotted as a function of temperature for RE-doped GZO films showed both metal-like and metal–semiconductor transition behaviour around a certain temperature point emphasized for each of the samples as follows.
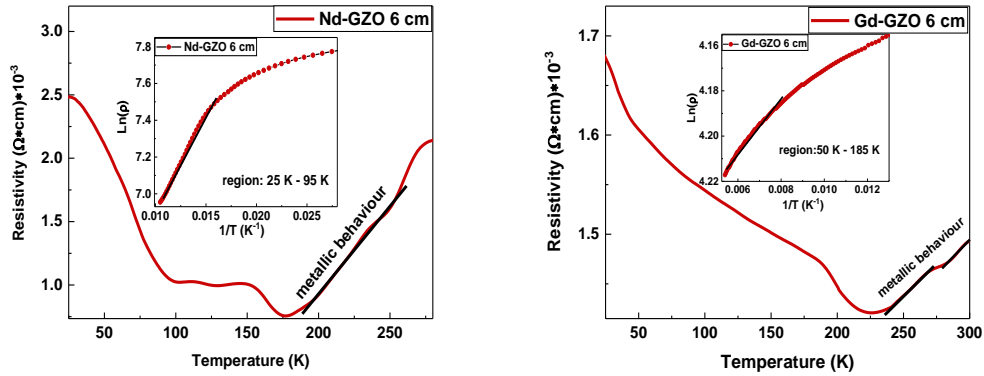
Fig.5.5.1 Temperature dependence of electrical resistivity of Nd-GZO, Gd-GZO thin film. The insert shows the curve fit of experimental for the semiconducting behaviour
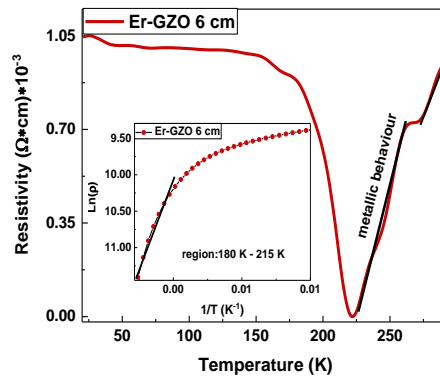

Fig.5.5.2 Temperature dependence of electrical resistivity of Er-GZO thin film. The insert shows the curve fit of experimental for the semiconducting behaviour

Resistivity measurements show the metal-like and metal–semiconductor transition behaviour of the films. These transitions can be divided into two distinctive regions for each measured film. Usually, the metallic behaviour is situated from room temperature until an absolute minimum, where the metal-semiconductor transition occurs. By further decreasing the temperature during the measurement, up to 20 K, all samples exhibit semiconducting behaviour.

By using the resistivity equation explained in chapter 2 (2.7.2), the resistivity values of the measured samples at room temperature are as follows: 0.155×10^{-3} Ω × cm for GZO film, while for the AGZO sample is 1.093×10^{-3} Ω × cm, 3.63×10^{-3} Ω × cm for Nd-GZO film, 14.31×10^{-3} Ω × cm for Gd-GZO sample and for Er-GZO sample the value is 5.23×10^{-3} Ω × cm. The shift of the critical temperature values for each

sample reveals the metal–semiconductor transition. This shift in resistivity could be assigned to decreasing trend of the grain size for that leads to considerable grain boundary effects that influence the electrical properties.

Doping with both Ga and RE elements lead to the addition of defects in the ZnO crystalline structure. This has a profound effect on the corresponding resistivity measurements, which indicates changes in the lattice symmetry and loss of crystalline quality.

Chapter 6. The study of ZnO nanoparticles doped with RE elements

6.1. Photoluminescence (PL) properties and Optical absorption results for RE-doped ZnO nanoparticles

Highlighted in Figure 6.1.1, the near band edge (NBE) around 380 nm and a predominant deep level emission (DLE) between 450 nm to 700 nm are observed. Moreover, the optical absorption results for RE-doped ZnO NP are also shown below.
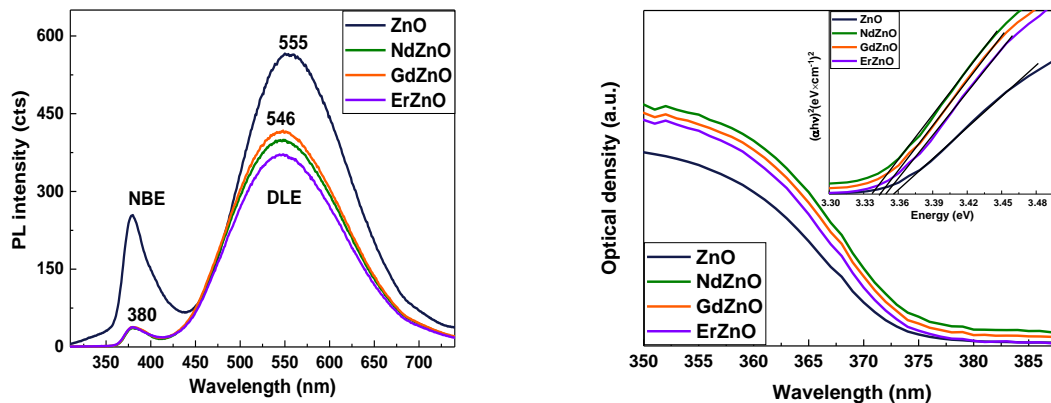

Fig.6.1.1 PL and Optical absorption spectra of the pristine ZnO and RE-doped ZnO nanoparticles. The insert in the 2nd spectra represents the Tauc plots of NP.

The different intensities of this NBE peak exhibit less exciton recombination for the doped ZnO NPs. A similar trend is kept in the spectral region related to the deep level emission (DLE) **[24]**. This green band from the visible range, around 555 nm, is usually attributed to many different kinds of defects such as OH defects attached at the surface of ZnO NPs by dangling bonds, oxygen vacancies, donor acceptor recombination, or antisite oxygen. Additionally, the difference in intensity of the NBE band compared to the DLE band most likely indicates that RE^{3+} ions act as non-radiative defects, the nature of which is different from the radiation defects responsible for the DLE band. Furthermore, there is a clear shift of the maximum of the emission peak from 555 nm to 546 nm with the incorporation of RE elements into the ZnO host material that may be attributed to donor–acceptor recombination or transition from the conduction band to oxygen antisite middle-gap levels.

From the absorption spectra, the optical band gap of the samples is determined by applying a linear fit in the Tauc coordinates for direct optical transition. The calculated values are relatively close to each other with a small variation between

3.35 eV for ZnO NPs to 3.33 eV for NdZnO NPs. This shift of the RE-doped ZnO samples indicates the narrow band gap may originate from the charge transfer between ZnO conduction band and the 4f or 5d electrons of RE that have an effective role in the electronic structure of ZnO.

6.2 Transmission electron microscopy (TEM) and selected area electron diffraction (SEAD) results for RE-doped ZnO nanoparticles

Figure 6.2.1 reveals the morphology and crystallinity of the nanocrystals determined using TEM. Representative microphotographs are presented in TEM images below, with well-defined facets and crystal lattice fringes of interplanar spacing d = 2.82 ± 0.05 Å corresponding to the (100) planes of hexagonal ZnO. Due to the morphology differences the diameter was evaluated between 3 nm and 7 nm.
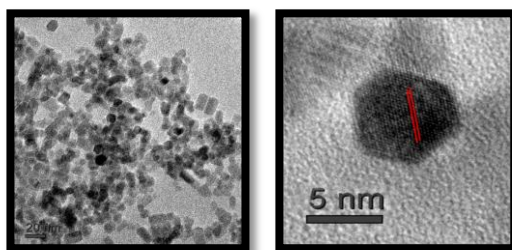

Fig. 6.2.1 TEM images upon distribution and shape of the ZnO nanoparticles. The spacing d = 2.82 ± 0.05 Å between the lattice fringes corresponds to the (100) planes of hexagonal ZnO structure

In order to determine the crystal phase patterns, SAED analysis was performed. In Figure 6.2.2, a set of concentric rings, typical for diffraction on an ensemble of randomly oriented NPs of very small dimension, is observed.
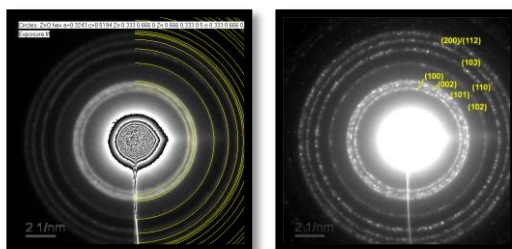

Fig. 6.2.2 SAED results upon the crystallinity of the ZnO nanoparticles

Indexing of the SAED pattern is assigned to the Miller indices (100), (002), (101), (102), (110), (103), and (200)/(112), respectively. This shows the high crystalline nature

of the samples. The calculated interplanar d-spacing distances of 2.80, 2.59, 2.46, 1.93, 1.63, 1.48, and 1.37 Å are characteristic for the hexagonal wurtzite ZnO structure (ICDD PDF card no. 36-1451). The lattice parameters calculated for the hexagonal structure, a = 0.324 nm and c = 0.519 nm.

6.3. The study of RE-doped ZnO nanoparticles by Raman spectroscopy

The role of excitons in the optical properties is further analysed by the multiphonon Raman spectra shown in Figure 6.3.1, where overtones of the longitudinal-optic (LO) phonon mode up to 2nd order in all the samples

The high intensity characteristic peak located at 574 cm^{-1} is assigned to the A$_1$(LO) phonon mode of ZnO NPs. Its high intensity measured with the resonant excitation of 325 nm (3.81 eV) is due to the strong electron-phonon interaction of the electronic states with the electric field of the polar (LO) phonon mode.
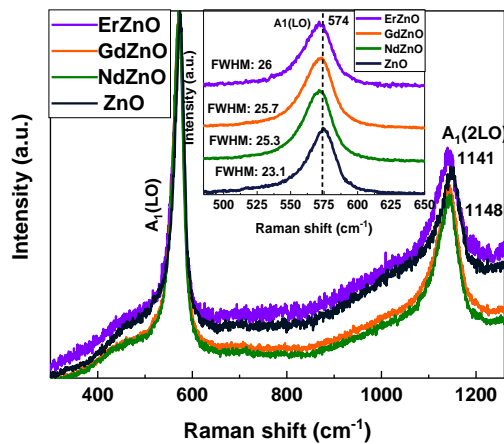
Fig.6.3.1 Raman spectra of pristine ZnO and RE-doped ZnO NPs measured in liquid form. The insert shows a zoom upon the shift and broadening of the 1st order peak

As compared to pristine ZnO NPs, with the addition of RE dopants, the peak position of the A$_1$(LO) mode shifts from 574 cm^{-1} to 571 cm^{-1}. In order to determine the full width at half-maximum (FWHM) of each peak, a Lorentz fit curve was used. For undoped ZnO NP, the A$_1$(LO) phonon peak has the FWHM about 23.1±0.4, while for RE-doped ZnO samples the values of FWHM vary as follows: NdGZO: 25.3±0.4, GdGZO: 25.7±0.4, and ErGZO: 26±0.4 as evidenced in the insert of figure above.

Final conclusions

Generally, a semiconductor material can be considered of having a geometrical shape that has a bulk and a surface, where the energy band structure will be affected by the boundaries of the material. As the size of a semiconductor decreases, the electrons will be more confined in the material leading to the quantum confinement effect resulting in increase of the energy gap of the bulk extended material. Furthermore, there will be an increase of the surface to the volume states. Additionally, there is an effect of dimentionality (1D, 2D, 3D shapes) of the material on the energy band structure, and they affect the energy band structure because of the quantum mechanical confinement. Therefore, such dependence has been used for producing specific effects in opto-electronic devices.

GZO, AGZO and RE-GZO thin films were grown using the RF magnetron sputtering technique on glass substrates by varying three distances between substrate and target. The structural, morphological, vibrational, optical and electrical properties of the films have been found to be influenced by the distance between substrate to target, as well as by the type of dopants used for the host material, ZnO.

XRD measurements confirm a hexagonal structure with a preferential orientation along the c-axis in the crystallographic direction [001] for pristine and Ga-doped ZnO. However, co-doping with both Ga and RE elements lead to non-epitaxial growth of the thin films. The substitution of RE^{3+} ions into the GZO structure has created a strong internal stress on the lattice due to the larger ionic radii of RE^{3+} ions, compared to the Ga-doped ZnO films. Regarding the stress inside the film structure, we observed the same compressive trend in all films.

AFM images emphasize a uniform and compact surface with spherical grains. The average roughness of the films is influenced by the type of dopants (Ga^{3+}, Al^{3+}, RE^{3+}) added to the ZnO host material.

Raman scattering analysis outlines that doping with Ga and co-doping with Al+Ga introduces $2B_{1(low)}$ band and lead to the increase of intensity for LO's band, suggesting the increase of oxygen vacancies. The shape of the optical combinations and optical-acoustic combinations were influenced the distance between substrate-target. The broad band due to the optical combinations, show for the GZO (d = 4 cm)

sample, two local maxima and for GZO (d = 8 cm) sample, one single asymmetric maximum. Meanwhile, co-doping with Ga and RE elements creates new vibration modes, and generates large amount of defects. Furthermore, results indicate the presence of (LO) modes up to four overtones and less intense peaks that are specific for the ZnO wurtzite structure and specific dopant vibration for some of the samples. It is strongly believed that the shift of the (LO) modes is due to strain/stress, which can occur due to RE-doping and/or due to scattering induced by defects (impurities and/or oxygen vacancies). This was previously confirmed by the XRD results.

Transmittance measurements reveal good transparency for all thin films, above 85%. Additionally, Er-doped GZO samples have the highest transparency compared to the other co-doped films. The optical band gap E_g was determined from the absorption spectra. Thus, the majority of samples show absorption above 3 eV. Comparing the E_g values of the pristine ZnO film, the GZO films and the AGZO films (from chapter 4), there is a decrease in the optical band gap values for the RE-GZO samples. The small increase in the band gap, E_g with increasing the distance between substrate-target is in agreement with the small increase of compressive strain. Due to the difference in valence and ionic radius of Zn^{2+} and RE^{3+}, the RE^{3+} ions can be incorporated from two pathways: inside the crystallites and at the grain boundaries. Compared with the pure ZnO film, the probable reason for increasing optical transmittance in doped-ZnO films can be due to occupied spaces in the ZnO by the doping ions, causing an increase in transmittance.

Resistivity measurements show the metal-like and metal–semiconductor transition behaviour of the films. These transitions can be divided into two distinctive regions for each measured film. Usually, the metallic behaviour is situated from room temperature until an absolute minimum, where the metal-semiconductor transition occurs. By further decreasing the temperature during the measurement, up to 20 K, all samples exhibit semiconducting behaviour. Depending on the nature of the dopant, the metal-semiconductor transition range was observed to shift from 170 – 175 K for the GZO film to 140 – 165 K for the AGZO film. XRD, AFM, Raman, transmittance and resistivity investigations corroborate increase in oxygen vacancies in doped samples.

To entail, co-doping (Ga+Al, Ga+RE) leads to additional defects in the ZnO crystalline structure. This has a profound effect on the corresponding resistivity measurements, which indicates changes in the lattice symmetry and loss of crystalline

quality. As a result, choosing the appropriate distance and percentage of the dopants can improve the structural, electrical, and optical properties of ZnO film, which is beneficial for transparent and conducting applications.

PL results revealed both excitonic and trap/surface PL bands. Luminescence in the visible region of the RE-doped ZnO NP consists of two distinct bands at around 380 nm (near band edge, NBE) and 550 nm (deep level emission, DLE). By comparing the pristine ZnO NPs with the RE-doped ZnO NPs, the PL spectra showed a blue-shift. Furthermore, the shift of the absorption edge in the optical absorption spectra of the RE-doped ZnO samples point out the narrowing of the band gap originating from the formation of oxygen vacancies and additional energy levels from the impurity atoms introduced into the wurtzite ZnO lattice.

TEM measurements show the distribution, crystallinity, shape, and the mean diameters of the NPs, resulting in a diameter between 3 nm and 7 nm, with a hexagonal shape. The selected area electron diffraction pattern reveals concentric rings that suggest the nanocrystalline nature of the particles and confirms the hexagonal wurtzite ZnO crystal structure with the specific lattice parameters $a = 0.324$ nm and $c = 0.519$ nm.

Raman analysis confirmed the wurtzite structure of RE-doped ZnO NPs. Overtones of the LO phonon mode (574 cm^{-1}) for ZnO NP and the deviated LO peaks of the RE-doped ZnO NP (571 cm^{-1}) were clearly determined. Morever, the overtones (2LO) present in the Raman spectra proved the crystallinity of the ZnO NPs, aspect that is in accordance with TEM results. The downward shifting of A_1(LO) mode for the RE-doped ZnO NPs are the evidence of the incorporation of RE^{3+} ions into the ZnO host material. Generally, it is agreed that this stress arises from a lattice mismatch and distortion. Therefore, doping with heavy elements is considered to be the main factor that would cause the lattice distortion of the crystals.

References

[1] M. Fowles, *Black carbon sequestration as an alternative to bioenergy*, Biomass and Bioenergy, 31, 426–432, **2007**. doi: 10.1016/j.biombioe.2007.01.012

[2] R. William, *Becquerel photovoltaic effect in binary compounds*, Journal of chemical physics, 32, **1960**. doi:10.1063/1.1730950

[3] M. A. Green, *Third generation photovoltaics: solar cells for 2020 and beyond*, Physica E, 14, 65–70, **2002**. doi:10.1016/s1386-9477(02)00361-2

[4] R. E. Smalley, *Future Global Energy Prosperity: The Terawatt Challenge*, MRS Bulletin, 30, 412–417**, 2005**. doi:10.1557/mrs2005.124

[5] A. Al-Omair Nuhad, Safenaz M. Reda, Farah M. Al-Hajri, *Effect of Organic Dye on the Photovoltaic Performance of Dye-Sensitized ZnO Solar Cell*, Advances in Nanoparticles, 3, 31–35, **2014**. doi: 10.4236/anp.2014.31005

[6] N. Thejo Kalyani, S. J. Dhoble, *Empowering the Future With Organic Solar Cell Devices,* Nanomaterials for Green Energy, 325–350, **2018**. doi:10.1016/b978-0-12-813731-4.00010-2

[7] U. Wurfel, A. Cuevas, P. Wurfel, *Charge Carrier Separation in Solar Cells*, IEEE Journal of Photovoltaics, 5, 461–469, **2015**. doi:10.1109/jphotov.2014.2363550

[8] S. K. Hau, H. L. Yip, N. S. Baek, J. Zou, K. O'Malley, A. K. Y. Jen, *Airstable inverted flexible polymer solar cells using zinc oxide nanoparticles as an electron selective layer*, Applied Physics Letters, 92, 253301, **2008**

[9] T. Alammar, A.V. Mudring, *Sonochemical Synthesis of 0D, 1D, and 2D Zinc Oxide Nanostructures in Ionic Liquids and Their Photocatalytic Activity*, ChemSusChem, 4,1796–1804, **2011**. doi:10.1002/cssc.201100263

[10] D. C. Reynolds, D. C. Look, B. Jogai, *Fine structure on the green band in ZnO*, Journal of Applied Physics, 89, 6189–6191, **2001**. doi:10.1063/1.1356432

[11] R. Ghosh Chaudhuri, S. Paria, *Core/Shell Nanoparticles: Classes, Properties, Synthesis Mechanisms, Characterization, and Applications*, Chemical Reviews, 112, 2373–2433, **2011**. doi:10.1021/cr100449n

[12] E. Roduner, *Size matters: why nanomaterials are different*, Chemical Society Reviews, 35, 583–592, **2006**. doi:10.1039/b502142c

[13] B. A. Gregg, M. C. Hanna, *Comparing organic to inorganic photovoltaic cells: Theory, experiment, and simulation*, Journal of Applied Physics, 93, 3605–3614, **2003**. doi:10.1063/1.1544413

[14] A. P. Alivisatos, *Semiconductor Clusters, Nanocrystals, and Quantum Dots,* Science, 271, 933–937, **1996**. doi:10.1126/science.271.5251.933

[15] A. E. Raevskaya, Y. V. Panasiuk, O. L. Stroyuk, S. Y. Kuchmiy, V. M. Dzhagan, A. G. Milekhin, D. R. T. Zahn, *Spectral and luminescent properties of ZnO–SiO2 core–shell nanoparticles with size-selected ZnO cores*, RSC Advances, 4, 63393–63401, **2014**. doi:10.1039/c4ra07959k

[16] V. V. Khomyak, M. M. Slyotov, I. I. Shtepliuk, G. V. Lashkarev, O. M. Slyotov, P.D. Marianchuk, V. V. Kosolovskiy, *Annealing effect on the near-band edge emission of ZnO,* Journal of Physics and Chemistry of Solids, 74, 291–297, **2013**. doi:10.1016/j.jpcs.2012.10.001

[17] S. Repp, E. Erdem, *Controlling the exciton energy of zinc oxide (ZnO) quantum dots by changing the confinement conditions*, Spectrochimica Acta Part A: Molecular and Biomolecular Spectroscopy, 152, 637–644, **2015**. doi:10.1016/j.saa.2015.01.110

[18] C. Lung, D. Marconi, **M. Toma**, A. Pop, *Characterization of the Aluminium Concentration upon the Properties of Aluminium Zinc Oxide Thin Films*, Analytical Letters, 491278–1288, **2016**. doi: 10.1080/00032719.2015.1094663

[19] A. Azarov, A. Galeckas, A. Hallén, A. Kuznetsov, E. Monakhov, B. G. Svensson, *Optical activity and defect/dopant evolution in ZnO implanted with Er*, Journal of Applied Physics, 118, 125703, **2015**. doi:10.1063/1.4931423

[20] R. Cebulla, R. Wendt, K. Ellmer, *Al-doped zinc oxide films deposited by simultaneous rf and dc excitation of a magnetron plasma: Relationships between plasma parameters and structural and electrical film properties*, Journal of Applied Physics, 83, 1087–1095, **1998**. https://doi.org/10.1063/1.366798

[21] A. Ganjoo, R. Golovchak, *Computer program PARAV for calculating optical constants of thin films and bulk materials: Case study of amorphous semiconductors*, Journal of Optoelectronics and Advanced Materials, 10, 1328–1332, **2008**.

[22] **M. Toma**, D. Marconi, M. Pop, C. Lung, A. Pop, *Influence of Substrate-Target Distance on Structural and Optical Properties of Ga and (Al + Ga)-doped ZnO Thin Films Deposited by Radio Frequency Sputtering*, Analytical Letters, 52, 2227–2238, **2019**.

[23] **M. Toma**, D. Marconi, C. Lung, O. Ponta, A. Pop, *Structural, morphological and optical properties of re-doped AZO thin films (RE=Nd, Gd, Er) grown by RF magnetron sputtering*, Studia Universitatis Babeș-Bolyai. Chemia. 60, 71–80, **2015**

[24] L. Honglin, L. Yingbo, L. Jinzhu, Y. Ke, *Experimental and first-principles studies of structural and optical properties of rare earth (RE = La, Er, Nd) doped ZnO*, Journal of Alloys and Compounds, 617, 102–107, **2014**. doi:10.1016/j.jallcom.2014.08.019